RESEARCH ARTICLE

INTERNATIONAL RESEARCH JOURNAL OF MULTIDISCIPLINARY TECHNOVATION

Asian Research Association

DOI: 10.54392/irjmt25612

Exploring Second-Order Nonlinear Optical Performance in Oxyquinolinium 3-carboxypropanoate: A Combined Experimental and DFT Study

R. Thirumurugan [a,*], K. Raju [a], K. Moovendaran [b], S. Raju [c], E. Shobhana [d]

[a] Department of Physics, Easwari Engineering College, Chennai-600089, Tamil Nadu, India.
[b] Department of Physics and Nanotechnology, SRM Institute of Science and Technology, Kattankulathur-603203, Tamil Nadu, India.
[c] Department of Physics, KPR Institute of Engineering and Technology, Coimbatore-641407, Tamil Nadu, India.
[d] Department of Physics, Kumaraguru College of Technology, Coimbatore-641049, Tamil Nadu, India
* Corresponding Author Email: beblissful006@gmail.com

DOI: https://doi.org/10.54392/irjmt25612

Received: 17-07-2025; Revised: 26-10-2025; Accepted: 07-11-2025; Published: 18-11-2025

Abstract: The crystallization of oxyquinolinium 3-carboxypropanoate (OXSU) was successfully achieved using a well-optimized slow evaporation approach. Although earlier experimental investigations have discussed its structural, thermal, and nonlinear optical (NLO) characteristics, the present study is a detailed computational analysis to clarify the electronic basis of its NLO response. X-ray diffraction (XRD) studies established the non-centrosymmetric (NCS) $P2_1$ crystal structure of OXSU, fulfilling the fundamental symmetry condition for second-order NLO activity. Hirshfeld surface (HS) analysis indicated that the intermolecular O–H···O/N–H···O hydrogen-bonding interactions were particularly important for stabilizing the acentric packing of OXSU for SHG activity. Vibrational spectroscopy (FTIR and FT-Raman) also provided evidence of both functional groups and hydrogen bonding interactions. Moreover, Mulliken charge analysis revealed evidence of charge redistribution during the formation of an asymmetrical charge density. Frontier molecular orbital (FMO) energy level calculations indicated an energy gap (ΔE = 3.82 eV) that encouraged intramolecular charge transfer (ICT). The molecular electrostatic potential (MEP) indicated regions of nucleophilic and electrophilic directions suggesting asymmetrical electron mobility. The material exhibits a high first hyperpolarizability (β = 16.94 × 10^{-30} esu), which is 33 times that of urea. The second harmonic generation (SHG) response is 30 % greater compared to potassium dihydrogen phosphate (KDP) and demonstrate phase-matchable behavior. This study documents the structure-property (SP) relationships in OXSU, correlating its acentric crystalline packing, hydrogen bonding interactions and charge transfer characteristics with NLO performance. These results establish that OXSU is a highly efficient, phase matchable organic NLO material with significant potential for optoelectronic applications.

Keywords: Organic NLO Single Crystal, Density Functional Theory, Hirshfeld Surface Analysis, Vibrational Studies, Optical Material, Phase Matchable Material.

1. Introduction

Nonlinear optical (NLO) materials continue to be extensively investigated due to its importance in next-generation photonic devices including optical communications, laser frequency conversion, optical switching, and data storage [1-3]. NLO materials, which exhibit phenomena particularly second-harmonic generation (SHG) and parametric oscillation, are the most popular owing to their potential to manipulate light at the molecular level [4, 5]. There are some advantages associated with organic NLO materials over inorganic materials, including their large hyperpolarizabilities, ultrafast response rates, and ease of tunability through molecular design [6, 7]. To design efficient organic NLO materials, π-conjugated systems with donor-acceptor (D-A) pairs are typically used to increase charge asymmetry and polarizability [8, 9]. Acentric crystal packing is a necessary requirement for second-order NLO activity, which guarantees a non-vanishing macroscopic nonlinearity. Hydrogen bonding also plays a role in providing directed, non-centrosymmetric (NCS) arrangements, helping to maintain specific orientations and supramolecular architectures [10, 11]. Proton transfer between acceptor and donor groups can give rise to zwitterionic or salt forms that tend to crystallize in NCS space groups, thus enhancing SHG activity [12, 13]. The interaction of π-π stacks with hydrogen bonds

has been intensively investigated in quinoline systems, as such molecules possess inherent asymmetry owing to their heterocyclic nature and protonation opportunity at the nitrogen atom [14-20]. Oxyquinoline (OQ) and its derivatives are of special interest because of their optoelectronic properties and versatile coordination chemistry. The OQ moiety owing to its electron-rich quinoline ring and hydroxyl group, easily complexes with organic and inorganic partners, resulting in often-enhanced NLO responses in the materials produced [21, 22]. 8-Hydroxyquinolinium maleate, for instance, has an SHG efficiency seven times higher than potassium dihydrogen phosphate (KDP) [23], and metal OQ complexes are commonly employed in organic light-emitting diodes (OLEDs) [24]. The 8-HQ succinate salt (8-HQSU), has already been synthesized and experimentally characterized as having encouraging properties, including high optical transmittance, 145°C thermal stability, and 1.3 times the SHG efficiency of KDP [25]. In order to understand how hydrogen bonding influences its acentric packing in OXSU and its NLO response (i.e., charge transfer), a theoretical foundation and electronic level insights is necessary. Density functional theory (DFT) is a valuable method for elucidating the electronic structure, vibrational dynamics, and NLO properties of molecular crystals. By correlating experimental findings with computational analyses, DFT can provide deeper insights into ICT, frontier molecular orbital (FMO) interactions, and hyperpolarizability, all of which govern NLO behavior [26]. For instance, Mulliken charge analysis and molecular electrostatic potential (MEP) plots reveal electron density redistribution, whereas Hirshfeld surface (HS) analysis quantifies the intermolecular interactions critical for crystal packing [27, 28]. In this study, we complemented the existing experimental characterization of OXSU [25] with a detailed computational investigation using DFT. We explored single-crystal X-ray diffraction (SCXRD) analysis to validate acentric crystalline architecture, HS analysis to delineate hydrogen-bonding networks, vibrational spectroscopy (FTIR, FT-Raman) to validate functional group assignments and hydrogen bonding, frontier molecular orbitals (FMOs) and MEP maps to assess charge transfer and reactivity, and first-order hyperpolarizability (β) calculations to rationalize the observed SHG response. Experiments and theoretical analyses should provide a more robust correlation between structure and properties of OXSU, emphasizing hydrogen bonding, molecular symmetry, and NLO properties. It is crucial to understand this process to rationally design the next-generation organic NLO materials.

2. Experimental Procedure

2.1 Material Synthesis and Crystal growth

OXSU was prepared by dissolving equimolar amounts (1 mmol) of OQ (1.45 g) in ethanol and a 1 mmol of 3-carboxypropanoic acid (1.18 g) in deionized water. The reaction mixture was prepared by mixing the two solutions with stirring for 2 h at room temperature. The crystalline product was obtained after filtration and dried under a perforated polyethylene film to control solvent evaporation. The first crystals appeared after 7 days and were purified by three recrystallizations from an ethanol solution. A saturated solution of purified OXSU in ethanol at 40°C was filtered, and the filtrate was evaporated very slowly at 28°C. After 8-10 days of controlled growth, optically transparent yellow crystalline blocks were formed and were selected for X-ray diffraction. The reaction scheme (Figure 1) confirms the proton transfer from succinic acid to the quinoline nitrogen, forming the oxyquinolinium 3-carboxypropanoate salt.

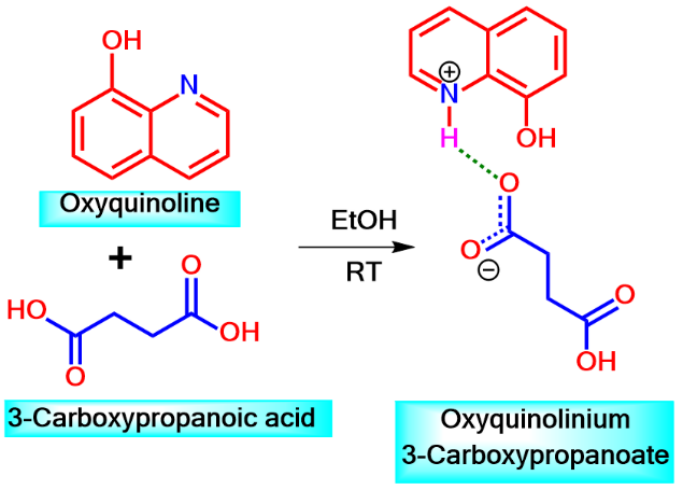

Figure 1. Scheme illustrating proton transfer reaction yielding OXSU

2.2 Characterization

The structural characterization of OXSU crystal was conducted with a ENRAF NONIUS CAD4 MACH3 diffractometer (Mo Kα radiation, λ = 0.7104 Å, graphite monochromator). A crystal (0.29 x 0.31 x 0.27 mm^3) has been mounted in the goniostat and centered. Unit cell parameters were obtained by indexing over 25 well-resolved reflections within the θ range of 9 ° and 11°. Cell refinement was achieved using the software CAD-4 EXPRESS [29]. The vibration properties of the OXSU sample were determined using FT-IR spectroscopy (JASCO FT/IR-410) in KBr pellets via mid-infrared (4000–400 cm^{-1}) region. Raman spectra of OXSU sample were recorded on a BRUKER RFS27 spectrometer equipped with 1064 nm Nd:YAG laser and scanning range was 4000–50 cm^{-1}.

3. Computational details

Optimization of the OXSU molecule was executed with the DFT using the B3LYP hybrid functional including Becke's three-parameter exchange (B3) and the Lee-Yang-Parr (LYP) correlation functional. The calculations were accomplished using Gaussian 09

[30] with 6-311++G(d,p) basis sets. Structural features, Mulliken charge distributions, MEP maps, and FMOs were evaluated with GaussView 6 [31]. The lowest-energy conformation was identified at the DFT/B3LYP/6-311++G(d,p) level. Additional analysis of Mulliken charges, FMOs, first-order hyperpolarizability, and NBO interactions was carried out on the optimized structure using the same approach. All simulations were carried out at the ground-state energy without any constraints on the potential energy surface.

4. Results and Discussion

4.1 Single-crystal X-ray diffraction analysis

SCXRD analysis demonstrated that OXSU is an active SHG monoclinic crystal in the NCS space group $P2_1$. Structural configuration is particularly significant because NCS arrangements are essential for SHG applications, which is evident from the potential of this material for NLO devices. The structural parameters demonstrated excellent consistency with the established crystallographic data [25] (Table 1), further validating the accuracy of the structural characterization.

4.2 NMR spectral studies

4.2.1 ^{1}H NMR spectrum

The ^{1}H NMR spectrum of OXSU (Figure 2 and Table 2) is dominated by the N-H$^+$ proton resonance at 14.29 ppm, reflecting strong hydrogen bonding to a 3-carboxypropanoate carboxylate oxygen. Quinolinium aromatic protons are observed at 7.74–9.48 ppm, and the most deshielded signals are at 9.48 ppm (C2-H) and 8.92 ppm (C4-H) corresponding to the ortho-position of the electron-withdrawing N$^+$ and C8-OH groups. In 3-carboxypropanoate, three distinct sets of methylene protons are observed. This indicates a significant difference in equivalence. This resonance is exceptionally deshielded (8.37–8.42 ppm, degeneration=3.0), suggesting that it may be close to the π-system of the quinolinium ring. A second resonance occurs at 6.08 ppm and a third one appears downfield (3.29 – 3.46 ppm). There is a large chemical shift dispersion in this aliphatic chain due to strong, inhomogeneous interactions between the anion and cation.

The calculated ^{13}C NMR spectrum of OXSU (Figure 3mand Table 3) distinctly separates carbonyl, aromatic and aliphatic domains. The carboxylate carbons of 3-carboxypropanoate anion are found at 182.58 ppm (C10) and 160.42 ppm (C13), revealing that it is asymmetrically hydrogen bonded to the cation. NMR chemical shifts for aromatic quinolinium carbons are in the range of 104.15 to 135.91 ppm. Deshielding of C3 can be attributed to its being bonded to both nitrogen and hydroxyl groups. The corresponding chemical shift appears at 135.91 ppm. By binding directly to the cationic nitrogen center, C8 displays a downfield resonance at 132.12 ppm.

Table 1. Lattice parameter values of the grown OXSU crystal

Lattice parameters	Reported [26]	Present work
a	9.549(1) Å	9.538(2) Å
b	4.974(5) Å	4.979(3) Å
c	12.678(8) Å	12.682(2) Å
β	104.04(5) °	104.07(3) °
Volume	584.2(7) Å^3	584.7(2) Å^3
System	Monoclinic	Monoclinic
Space group	$P2_1$	$P2_1$

Table 2. DFT-GIAO calculated ^{1}H NMR chemical shifts and assignments for OXSU

Proton Label	**δ (ppm)**	**Assignment**
H8	14.29	Quinolinium N-H$^+$
H3	9.48	Quinolinium C2-H
H1	8.92	Quinolinium C4-H
H5, H2, H4	8.37 - 8.42	Succinate CH_2
H6	8.14	Quinolinium C5-H / C6-H
H13	7.74	Quinolinium C5-H / C6-H
H7	6.08	Succinate CH_2
H11, H12, H9, H10	3.29 - 3.46	Methylene Protons (Succinate)

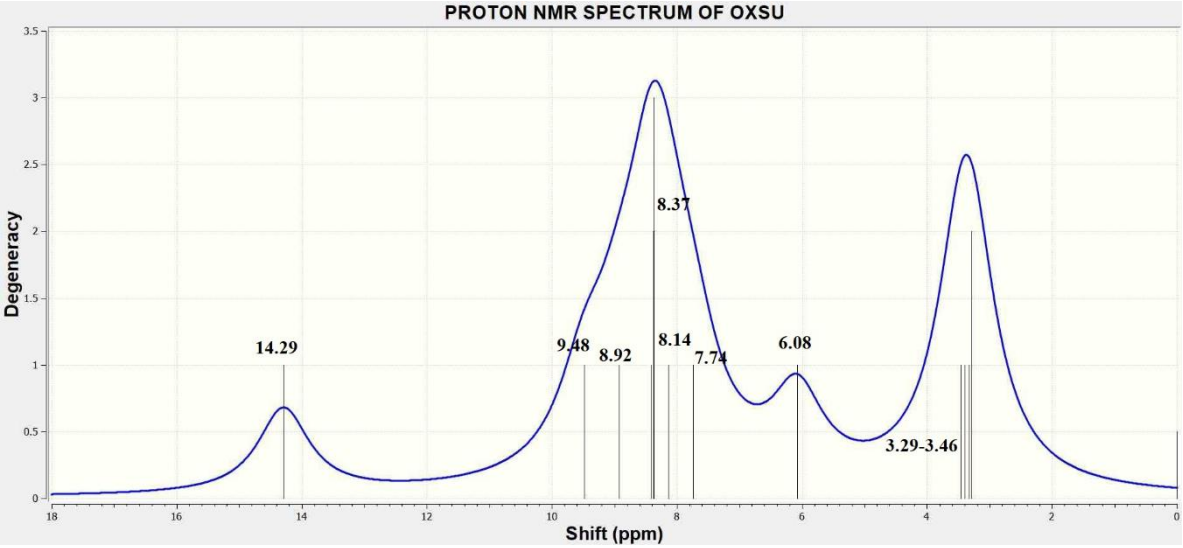

Figure 2. DFT-GIAO computed ^{1}H NMR spectrum of OXSU molecule

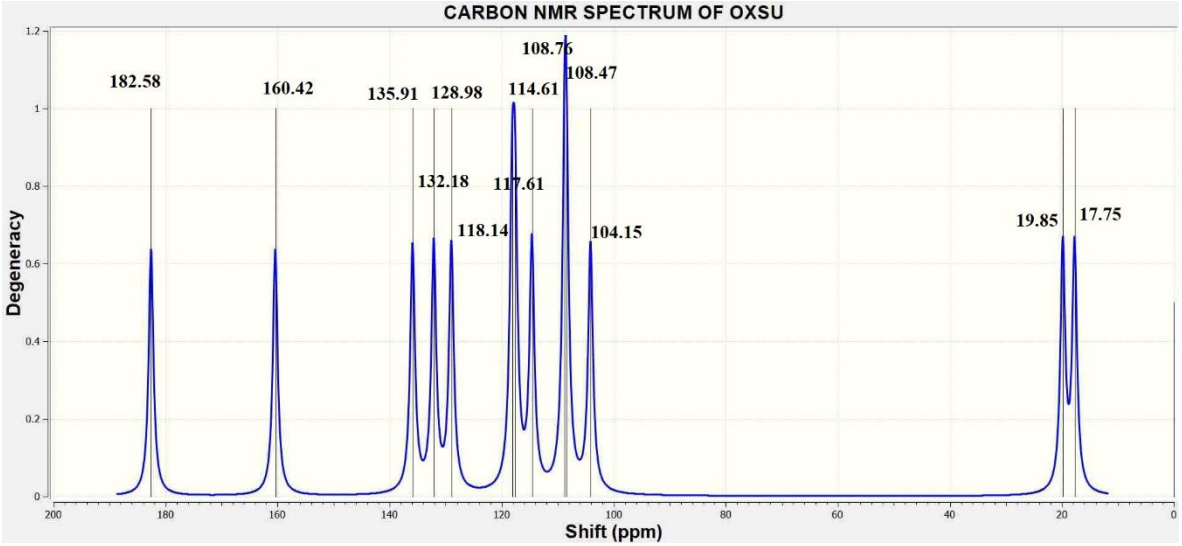

Figure 3. DFT-GIAO computed 13C NMR spectrum of OXSU molecule

Table 3. DFT-GIAO calculated ^{13}C NMR chemical shifts and assignments for OXSU

Carbon Label	δ (ppm)	Assignment
C10	182.58	Succinate COO^-
C13	160.42	Succinate COO^-
C3	135.91	Quinolinium C4
C8	132.12	Quinolinium C2
C1	128.98	Quinolinium C4
C4	118.14	Quinolinium C5/C7
C6	117.61	Quinolinium C6
C9	114.61	Quinolinium C3
C5	108.76	Quinolinium C8
C2	108.47	Quinolinium C8
C7	104.15	Quinolinium C8
C11	19.85	Succinate CH_2
C12	17.75	Succinate CH_2

Furthermore, C1 carbon, ortho to both N^+ and OH generates a resonance at 128.98 ppm. In the 3-carboxypropanoate moiety, methylene carbons (C11 and C12) are also strong non-equivalents due to resonance at 19.85 and 17.75 ppm, respectively. Hydrogen bonding stabilises this asymmetric ionic environment causing the shift difference.

4.3 Hirshfeld Surface Analysis

Hirshfeld surface (HS) analysis partitions electron density in molecular crystals to define molecular domains, facilitating studies of intermolecular interactions and packing arrangements [32]. The key distance parameters characterizing the HS include d_i (distance from a surface point to the closest nucleus inside its domain), d_e (distance to the closest nucleus outside its domain), and the normalized contact distance d_{norm}. Fingerprint (FP) plots provide a complementary visualization. Specifically, d_{norm} is used to locate and quantify the strength of close intermolecular contacts across the surface.

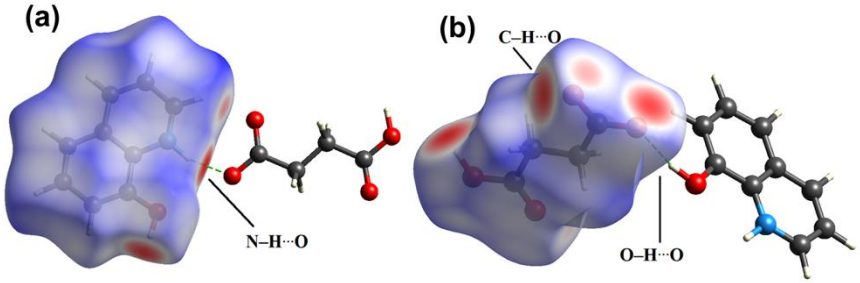

Figure 4.(a),(b) Two different orientations of Hirshfeld surface mapped with d_{norm} (red represents the closest contact, and blue represents the most distant contact).

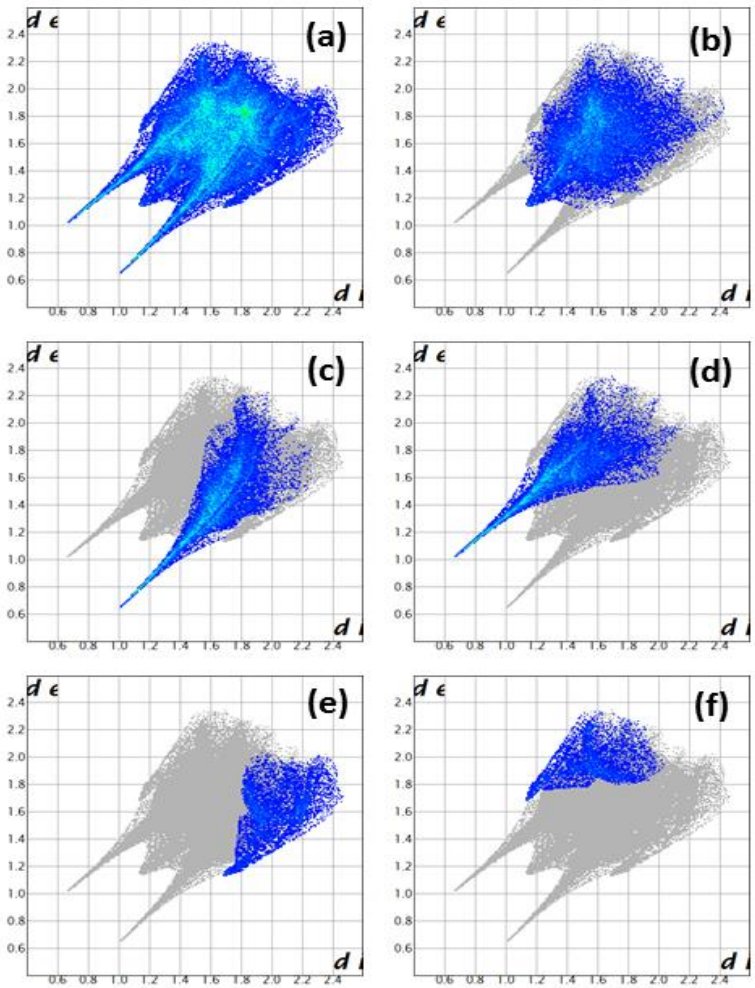

Figure 5. Fingerprint plots of **(a)** all interactions, **(b)** H···H (33.1 %), **(c)** O···H (23.3 %), **(d)** H···O (20.4 %), **(e)** C···H (8.8 %) and **(f)** H···C (6.8 %) interactions

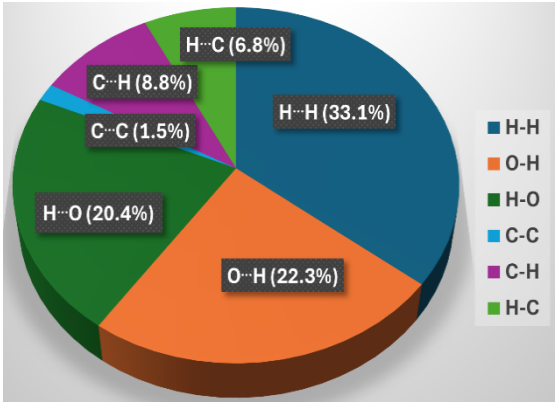

Figure 6. Percentage of intermolecular interactions involved in OXSU crystal.

$$d_{norm} = \frac{d_i - r_i^{vdW}}{r_i^{vdW}} + \frac{d_e - r_e^{vdW}}{r_e^{vdW}} \quad (1)$$

The van der Waals (vdW) radii of the two atoms inside and outside the surface are represented by r_i^{vdW} and r_e^{vdW}, respectively. While red color indicates strong interactions (vdW< d_{norm}) and blue color indicates weak interactions (vdW > d_{norm}).

The HS analysis (Figure 4) and the respective 2D FP plots (Figure 5a-f and figure 6) of OXSU offer the essential intermolecular interactions that prevail in the crystal packing, which are responsible for the NLO response in acentric crystals. The H···H contacts (1.467 Å) dominated (33.1%) the HS and suggested strong van der Waals interactions, which played a key role in the compact molecular packing (Figure 5b). This is common for organic cocrystals, in which the large contribution of dispersion forces is the dominant factor in the stabilization of the crystal lattice. The O···H (22.3%) and H···O (20.4%) contacts prove that strong N–H···O and O–H···O hydrogen bonds mainly contribute to the stabilization the crystal. These O···H and H···O interactions are represented by sharp spikes in the bottom right (Figure 5c) and top left regions (Figure 5d) of the FP plot, respectively. These interactions are reflected in the high and localized peaks in the FP plots, which are typical of directional hydrogen bonding. The 3-carboxypropanoate anion and oxyquinolinium cation led to a strong hydrogen-bonded network that reinforced the acentric packing required for second-order NLO applications. Additionally, the C···H (8.8%) and H···C (6.8%) interactions indicate weaker but structurally relevant C–H···O contacts, that contribute to the molecular packing. These C···H and H···C interactions are reflected in the bottom right area (Figure 5e) and top left region (Figure 5f) of the FP plots. Although less dominant than primary hydrogen bonds, these interactions support the three-dimensional network and augment crystal cohesion. The asymmetric arrangement of interactions, specifically the strong O–H···O and N–H···O hydrogen bonds, as well as the lack of a center of inversion correspond to the requirements for SHG. The large number of H···H contacts indicate effective packing, and the directional hydrogen bonds guarantee a NCS pattern, which is crucial for NLO activity. The HS analysis clearly indicated that OXSU was stabilized mainly by N–H···O and O–H···O hydrogen bonding, along with C–H···O and van der Waals interactions. Acentric crystal packing is facilitated by this balanced interplay of strong and weak interactions, thus OXSU is a potential candidate for the second-order NLO applications [33]. Further investigations into hyperpolarizability and SHG efficiency of this compound were conducted to access its suitability.

4.4 Vibrational studies

The experimental spectra of vibrations from OXSU were recorded by using FTIR (Figure 7b) and FT-Raman (Figure 8b) spectroscopic methods. The theoretical frequency of vibration (Table 4) was determined using density functional theory (DFT) at the B3LYP/6-31G(d,p) level. The results of DFT calculated frequencies are compared with the spectrums obtained from experiments. The comprehensive spectrum analysis reveals that N-H···O and O-H···O interactions supports the development of a proton transfer complex within the compound.

4.4.1 O-H Stretching Vibrations

The O-H stretching vibrations can be detected on the scale of 3672 cm^{-1} (DFT) and 3459 cm^{-1} (FTIR). These vibrations are related to hydroxyl groups that are present in both oxyquinolinium and 3-carboxypropanoate portions in the molecules [34]. The slight shift that is observed in the spectra from experiments indicates the possibility of hydrogen bonds in the crystalline form that could affect the frequency of vibration.

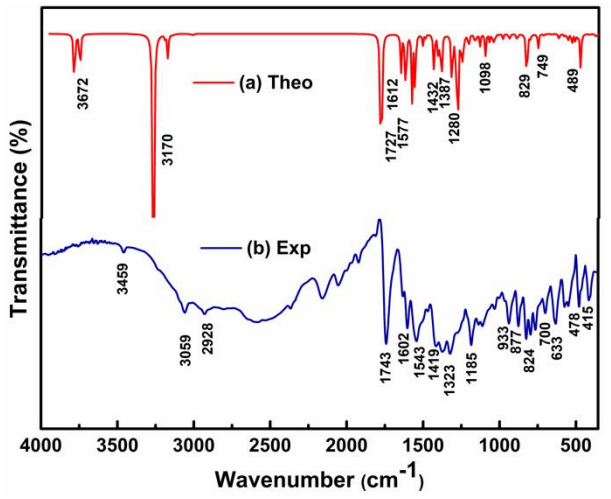

Figure 7. FTIR spectra of OXSU molecule **(a)** theoretical **(b)** experimental

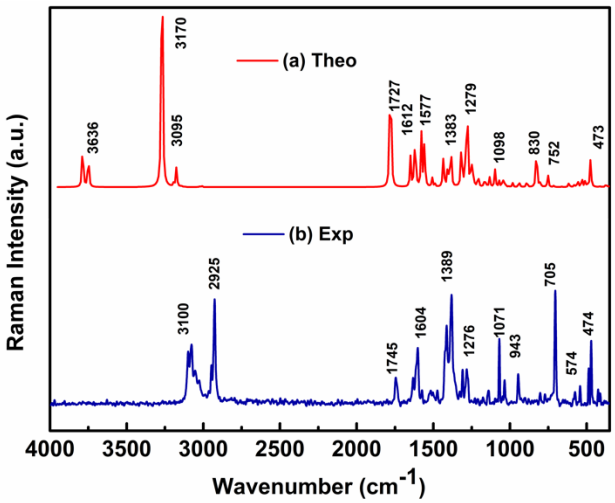

Figure 8. FT-Raman spectra of OXSU molecule **(a)** theoretical **(b)** experimental

Table 4. The calculated and observed vibrational wavenumber (cm^{-1}), and the corresponding vibrational assignments of OXSU

S.No.	Calculated wavenumber		Observed wavenumber		Vibrational assignments with PED (%)
	Unscaled	Scaled	FTIR	FT-Raman	
1	3825.37	3672.36			v O-H (100) (8HQ)
2	3787.93	3636.41	3459(w)		v O-H (100) (succinate)
3	3302.25	3170.16			v N-H (98)
4	3224.05	3095.09		3100(s)	v C-H (89) (8HQ aromatic)
5	3207.33	3079.04		3079(s)	v C-H (96) (8HQ aromatic)
6	3206.77	3078.5			v C-H (90) (8HQ aromatic)
7	3194.3	3066.53			v C-H (93) (8HQ aromatic)
8	3188.44	3060.9	3059(w)	3050(w)	v C-H (94) (8HQ aromatic)
9	3176.04	3049		3030(w)	v C-H (93) (8HQ aromatic)
10	3101.54	2977.48			v_{as} CH2 (96) (succinate)
11	3076.49	2953.43		2945(w)	v_{as} CH2 (94) (succinate)
12	3055.03	2932.83	2928(w)	2928(s)	v_{sy} CH2 (96) (succinate)
13	3040.12	2918.52			v_{sy} CH2 (98) (succinate)
14	1799.64	1727.65	1743(s)	1745(s)	v C=O (83) (carboxylic acid succinate)
15	1669.74	1649.7	1632(w)	1634(w)	v C-C (33) (8HQ ring), β HNC (10)
16	1643.25	1623.53			v C-C (32) (8HQ ring)
17	1632.16	1612.57	1602(s)	1604(s)	v_{asy} COO-(70)
18	1596.98	1577.82		1573(w)	β HNC (15), β HCC (28)
19	1576.63	1557.71	1543(s)	1517(w)	v_{sy} COO-(70), v C-C (20) succinate
20	1526.04	1507.73			β HCC (14)
21	1507.47	1489.38	1468(w)	1473(w)	β HCC (31)

22	1454.8	1437.34			δ_{sci} CH2(89)
23	1453.02	1435.58			β HCC (63)
24	1449.39	1432	1419(w)	1415(s)	δ_{sci} CH2(86)
25	1422.62	1405.55			v C-C (24) (8HQ ring), β CNC (11)
26	1404.44	1387.59			v C-O (11), v C-C (12), τ HCCO (27)
27	1399.94	1383.14	1376(w)	1383(s)	v C-C (31), v C-N (13) (8HQ ring)
28	1369.75	1353.31	1323(m)	1309(s)	w CH2 (36), τ HCCO(32) succinate
29	1332.77	1316.78			v O-C (16), v C-C (10), β HCC (18)
30	1309.83	1294.11		1276(m)	v N-C (14), v O-C (14), β HCC (25)
31	1294.92	1279.38			v O-C (21), β HOC (33), τ HCCO(12)
32	1268.07	1252.85			v N-C (13), v C-C (10), β HOC (22), β HCC (11)
33	1260.21	1245.09			β HCC (15), τ HCCO (45)
34	1252.04	1237.02			v C-C (13), v C-N (21), β HCC (37)
35	1223.01	1208.33			β HCC (49)
36	1221.34	1206.68			β HCC (20)
37	1184.5	1170.29	1185(w)	1175(m)	β HOC (25), β HCC (43)
38	1173.58	1159.5	1137(w)	1137(w)	v O-C (31), β HOC (38) succinate carboxylic acid
39	1170.95	1156.9			v C-C (18), β HCC (52) 8HQ
40	1146.73	1132.97			ν_{as} COO- (77)
41	1111.43	1098.09	1111(w)		v O-C (14), v C-C (10), β CNC(12), β HCC (22)
42	1083.58	1070.58		1071(s)	v C-C (38) 8HQ
43	1060.61	1047.88	1033(w)	1037(m)	v C-C (35) 8HQ
44	1057.31	1044.62			v C-C (51) succinate
45	1044.9	1032.36			τ HNCC(26), τ HCCC(47)
46	1018.82	1006.59			τ HCCC(83), τ CCCC (12) 8HQ
47	995.18	983.238			τ HCCC(69), τ CCCC (15) 8HQ
48	994.29	982.359			v C-C (10), β HCC (13), τ CCCO (10) 8HQ
49	953.26	941.821			τ HNCC(13)
50	947.27	935.903	937(m)	943(s)	τ HNCC(31), τ HCCC(46)
51	903.57	892.727			τ HCCC(77)
52	900.3	889.496	877(m)		β CCC (24) succinate, β NCC (29) 8HQ
53	839.15	829.08	824(m)		τ HCCC(28)
54	836.26	826.225			v C-C (26)
55	832.44	822.451			v C-C (52)
56	811.48	801.742			β CCC (70) 8HQ
57	786.87	777.428	796(w)	803(m)	τ HCCC(55), t OCCC (12) 8HQ (aromatic C-H OPB)
58	761.34	752.204	765(w)	767(w)	τ HCCC(37), τ CCCC (10), τ CNCC (11) aromatic C-H OPB
59	722.36	713.692			β CCC (31) 8HQ ring ipb

60	670.42	662.375	700(w)	705(s)	β OCC (31), t OCOC (18) opb succinate carboxylate
61	628.38	620.839	633(s)		τ NCCC(11), τ CCCC (16), τ CNCC (19), t OCCC(13) succinate
62	622.32	614.852			δsci COO- (35), t OCOC (14) succinate
63	587.37	580.322		574(w)	t OCOC (54)
64	585.64	578.612			β CCC (36) 8HQ RING IPB
65	564.86	558.082	551(w)		τ HOCC (28), τ HCCO (16), t OCOC (21) succinate
66	542.41	535.901			β CCC (50), β OCC (14) succinate
67	535.82	529.39	547(w)		δ_{sci} COO- (34), τ HCCO(13), t OCOC (14)
68	515.02	508.84			β CCC (18), τ HCCO (10), t OCOC (33)
69	495.19	489.248	479(s)	490(s)	β CCC (40) ipb OQ ring
70	479.71	473.953		467(s)	τ HOCC (62), τ HCCO (10), t OCOC (12)
71	470.46	464.814			τ NCCC(25), τ CCCC (36)
72	468.92	463.293			ν C-C (12), β OCC (29)
73	420.26	415.217	415(m)	424(m)	τ HCCC (13), τ CNCC(27), t OCCC (14) OQ ring
74	377.96	373.424		408(w)	ν C-C (12), β OCC (25), β OCO (25), β CCO (16) succinate
75	325.58	321.673			τ HOCC(92) 8HQ
76	275.4	272.095			β CCC (37), β OCC (24)
77	269.81	266.572			β CCC (39), β OCC (29)
78	266.26	263.065			τ CCCC (45), t OCCC (16)
79	202.37	199.942			β CCC (43), β OCC (34)
80	174.53	172.436			τ CCCC(32), t CCCC (33)
81	161.39	159.453			τ NCCC(11), τ CCCC (31)
82	139.45	137.777			ν O-H (10), t CCCC (55) succinate
83	103.98	102.732			ν O-H (55), t CCCC (19) succinate
84	67.29	66.4825			β COH(20), τ OCCC(26), τ CCOH (19) succinate
85	64.64	63.8643			β OHN (11), τ CCOH (46)
86	50	49.4			τ OHNC (16), t CCCO (26)
87	40.32	39.8362			β OHN (60)
88	33.6	33.1968			τ OHNC (27), τ OCCC (14), τ CCCO (16)
89	20.69	20.4417			τ OHNC (10), τ COHN (54)
90	19.55	19.3154			β COH (44), τ COHN (18)

δ – deformation; τ – torsion; β- in plane bending; opb- out of plane bending; sci – scissoring; ω – wagging; ρ – rocking; ν –stretching; ν_s – symmetric stretching; ν_{as} – asymmetric stretching; w – weak; m –medium; s – strong.

4.4.2 C-H Stretching Vibrations

The C-H stretching patterns within the OQ aromatic rings can be observed in the range between 3095-3049 cm^{-1} in theoretical spectrum. The frequencies measured by the theoretical are in good agreement with experimental results of 3079, 3050, 3030 (FT-Raman) cm^{-1} and 3059 (FT-IR) cm^{-1}. The close correlation between these frequencies suggests that the C-H stretches that are aromatic are

primarily dependent on intramolecular interactions in the OQ ring. The minor shifts caused by interactions between molecules.

4.4.3 N-H Stretching Vibrations

It is believed that the stretch of N-H vibration can be observed in the range of 3170 cm^{-1} in the theoretical spectrum that corresponds with the quinolinium (N-H) stretch. Since powerful interactions that occur in the crystalline state, this frequency mode exhibits weakness in spectrum. The N-H group is essential to this proton transfer procedure because the quinolinium nitrogen could be involved in hydrogen bonds to carboxylate oxygen of the 3-carboxypropanoate group.

4.4.4 C=O Stretching (Carboxyl Group)

The C=O stretching frequency in the carboxyl groups of 3-carboxypropanoate is visible at 1743 cm^{-1} and 1745 cm^{-1} on the FTIR and FT-Raman spectrum, and the DFT computations predict the type of vibration to be 1727 cm^{-1} [35, 36]. The red shift seen in the experiment data suggests that the C=O stretching is influenced through intermolecular interactions. It is due to the hydrogen bonds between the O-H group (from OQ) and the C=O group (from 3-carboxypropanoate). This is in line with the expected hydrogen bonding and the construction of the proton transfer complex.

4.4.5 C-C and C-N Stretching Vibrations

The C-N and C-C stretching vibrations in the quinolinium ring can be observed in the range of 1632 cm^{-1} (FTIR) as well as 1634 cm^{-1} (FT-Raman). These DFT-scaled frequencies for the two types correspond to 1649 cm^{-1} (C-C) and 1623 cm^{-1} (C-N) and confirm the quinoline-ring coupling [37]. The stretching patterns are affected by potential proton transfer process from the 3-carboxypropanoate group to the nitrogen quinolinium.

4.4.6 Carboxylate group vibrations (COO^- stretching)

The stretching asymmetric and symmetric mode of carboxylate group (COO^-) are observed at 1602 cm^{-1} (FTIR), 1604 cm^{-1} (FT-Raman) and 1543 cm^{-1} (FTIR), 1517 cm^{-1} (FT-Raman). Its DFT-scaled frequencies for these modes are 1612 cm^{-1} (asymmetric) and 1557 cm^{-1} (symmetric). These vibrations are attributed to the COO^- asymmetric and symmetric stretch. The symmetric stretch contributes more (70 % PED) to the overall vibrational profile. The observed shifts in FTIR and FT-Raman spectra verify this interaction of the hydrogen bonds among both the carboxylate oxygen and the quinolinium nitrogen.

4.4.7 N-H···O and O-H···O interactions

One of the most important characteristics of OXSU is its possibility of hydrogen bonding interactions as well as proton exchange between the endocyclic nitrogen in OQ and the carboxylate groups of 3-carboxypropanoate. The observed vibrational patterns including the O-H stretching at 3459 and 3672 cm^{-1}, as well as the N-H stretching at 3170 cm^{-1} could indicate that there is a possibility for N-H···O or O-H···O interactions [38]. These interactions may be revealing a proton transfer complex development between single quinolinium nitrogen along with oxygen and the 3-carboxypropanoate carboxylate oxygen. This is further confirmed with these shifting of the red seen within the C=O stretching mode, which confirms the development of a hydrogen-bonded structure.

4.4.8 CH_2 deformation and torsion (3-carboxypropanoate)

The CH_2 deformations and torsional vibrations within the 3-carboxypropanoate group can be observed around 1419 cm^{-1} (FTIR) as well as 1415 cm^{-1} (FT-Raman) and are attributed to CH_2 scissoring as well as torsional modes. These DFT calculations predicted these modes at 1432 cm^{-1} which is a significant contribution in 3-carboxypropanoate group.

4.4.9 Other vibrational modes

The C-C and C-N bending modes can be observed at 1276cm^{-1} in FT-Raman and predicted to be 1294 cm^{-1} using DFT-scaled calculations [35]. These vibrations are derived from the quinolinium ring and are coupled to 3-carboxypropanoate interactions. C-H torsion and bending models in the OQ ring have been seen at 765 cm^{-1} (FTIR) and 767 cm^{-1} (FT-Raman) in the in line with DFT predictions.

4.5 Second Harmonic Generation (SHG) Response

SHG efficiency of OXSU was quantified using a modified Kurtz-Perry powder method. OXSU crystals were sieved into a uniform particle size (120-150 µm) and loaded into a microcapillary tube and compared relative to a KDP standard with equivalent particle dimension. For excitation a Q-switched Nd:YAG laser source (λ = 1064 nm) delivering 10 ns pulses with an energy of 5.7 mJ was employed. The emitted SHG signal at 532 nm was spectrally isolated using a monochromator and a BG-38 optical filter to eliminate any residual fundamental wavelength. Signal detection was carried out using a Hamamatsu R2059 photomultiplier tube coupled with a TDS 3052B 500 MHz oscilloscope for real-time visualization.

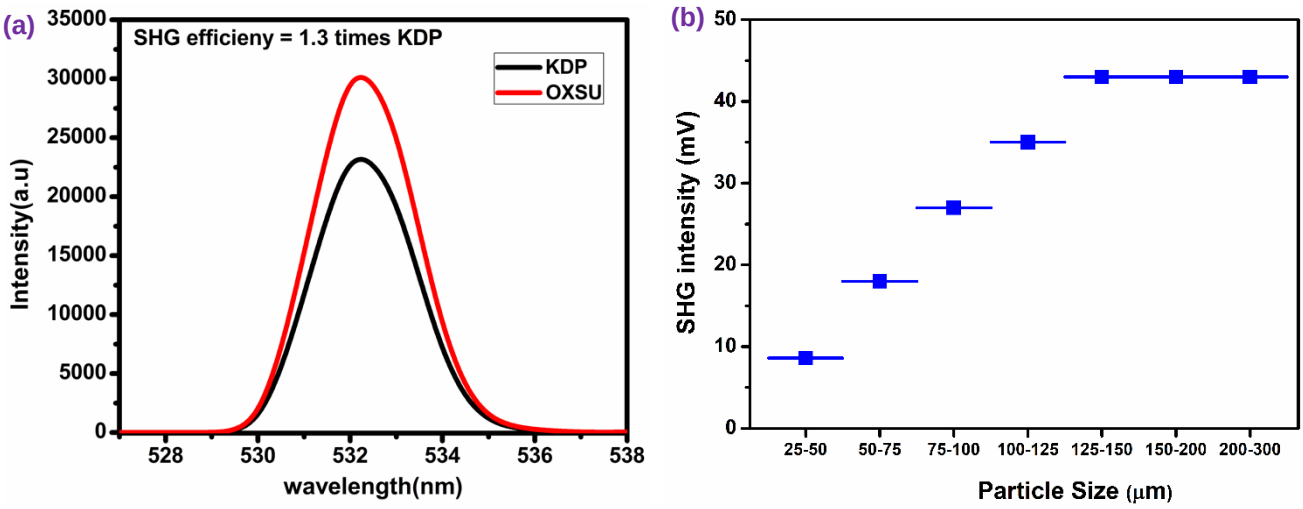

Figure 9a. The powder SHG signals of KDP (black colour) and OXSU (red colour), **b.** Particle size dependence powder SHG output of OXSU.

The SHG output from OXSU was found to be 43 mV which is significantly enhanced compared to 34 mV obtained for KDP (Figure 9a). This corresponds to a relative SHG efficiency of approximately 1.3-fold greater. This improved performance is directly linked to the molecular and crystalline features of OXSU. Molecularly, OXSU is characterized by an ICT system, where the electron density flowing from oxyquinolinium donor to 3-carboxypropanoate acceptor [39]. The π-conjugated quinoline framework facilitates ICT resulting in improved electron delocalization and hyperpolarizability (β), key contributors to efficient SHG response [40]. The key N–H···O and O–H···O hydrogen bonds reinforce the lattice and facilitate extended charge delocalization for achieving phase-matching conditions [41]. The particle size-dependent SHG measurements were performed to confirm the phase-matchable behavior of OXSU crystal. The results (Figure 9b) obviously demonstrate that a significant increase in SHG intensity for increasing particle size ranges from 0-50 μm to 150-200 μm followed by saturation. This correlation is a characteristic signature of a phase-matchable material. These non-covalent interactions also promote acentric molecular arrangement required for effective NLO functionality [42]. The synergistic contribution of asymmetric crystalline packing, efficient ICT, π-electron delocalization, and directional hydrogen bonds establish the strong SHG response of OXSU, positioning its potential for advanced photonic technologies.

4.6 Optimized molecular geometry

The optimized geometry of OXSU was depicted along with atom numbering scheme is shown in Figure 10. Table 5 summarizes the comparison between SCXRD-derived geometrical parameters (bond lengths, angles, torsion angles) and those calculated for OXSU at the DFT/B3LYP/6-311++G(d,p) level. No significant deviations were observed in the bond lengths values. Similarly, most bond angles and torsion angles values in the DFT structure closely matched the experimental values, except carboxylate group (O2—C10—O3). The bond angles O2—C10—O3, O2—C10—C11 and O3—C10—C11 deviate by 11.40 °, 3.23 ° and 8.15 °, respectively. Thus, C13—C12—C11—C10, O2—C10—C11—C12 and O3—C10—C11—C12 dihedral angles show deviations of 117.8 °, 17.1 ° and 16.7 °, respectively. The backbone (C13—C12—C11—C10) of 3-carboxypropanoate anion moiety in the calculated OXSU structure showed the largest deviation (117.8 °) from experimental values. These discrepancies between the DFT-optimized structure and SCXRD are consistent with expected differences between gaseous state computational results and the solid phase experimental measurements [43]. The structural deviations were evaluated using RMSD formula. While bond lengths (0.032 Å) and angles (0.65 °) demonstrated high reliability to SCXRD data, torsion angles showed significant divergence (RMSD = 2.78 °).

$$\text{RMSD} = \sqrt{\frac{1}{N-1}\sum_{i}^{N}(\Upsilon_i^{\text{Theo}} - \Upsilon_i^{\text{XRD}})} \quad (2)$$

4.7 Mulliken Atomic Charge Distribution Analysis

Mulliken charge analysis supports the structural features determined by the crystallography and emphasizes the importance of hydrogen bonding in increasing the NLO activity of the compound. Figure 11 represents distribution of Mulliken charges computed for OXSU and listed with values in Table 6. The electronegative oxygen (O1-O4) and nitrogen (N1) atoms exhibited characteristic negative charges. The carbon atoms located in oxyquinolinium cation showed both positive (C1, C2 and C7) and negative (C3, C4, C5, C6, C8 and C9) charge distributions. This occurrence of π-conjugation over the quinoline ring results in enhanced the NLO activity in OXSU.

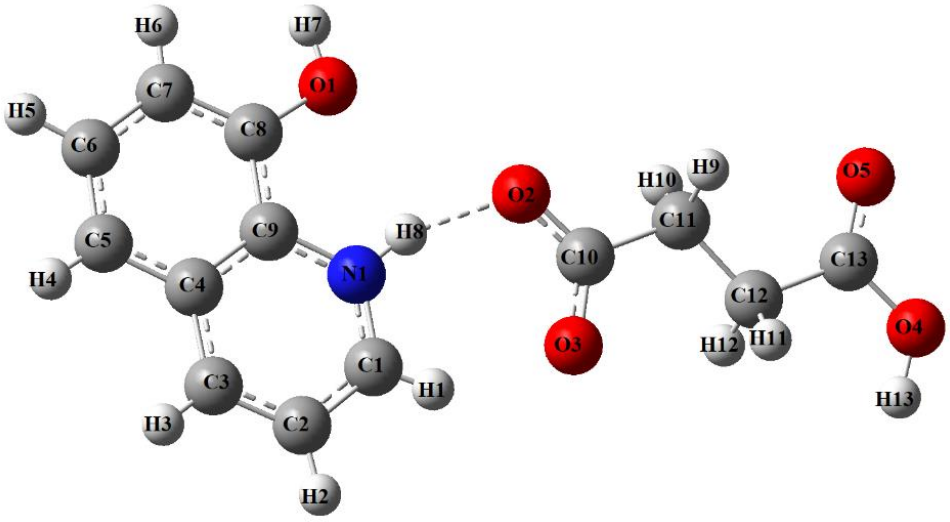

Figure 10. The optimized molecular structure of OXSU by DFT/B3LYP method with 6-311++G (d,p) basis set.

Table 5. Comparison of DFT/B3LYP/6-311++G(d,p) structure of OXSU against SCXRD geometries

Parameters	**(XRD)**	**6311++ G(d,p)**
Bond length values (Å)		
O(5)-C(13)	1.324(3)	1.339
O(2)-C(10)	1.247(3)	1.264
O(3)-C(10)	1.257(3)	1.252
O(1)-C(6)	1.344(3)	1.355
O(4)-C(13)	1.200(3)	1.210
N(1)-C(8)	1.320(3)	1.331
N(1)-C(7)	1.365(3)	1.370
C(7)-C(2)	1.414(3)	1.422
C(7)-C(6)	1.420(3)	1.416
C(2)-C(3)	1.404(4)	1.416
C(2)-C(1)	1.414(3)	1.415
C(6)-C(5)	1.361(3)	1.378
C(5)-C(4)	1.404(4)	1.412
C(12)-C(13	1.504(3)	1.518
C(12)-C(11)	1.505(3)	1.530
C(10)-C(11)	1.518(3)	1.500
C(1)-C(9)	1.364(4)	1.379
C(9)-C(8)	1.396(4)	1.397
C(3)-C(4)	1.359(3)	1.374
Bond angle values (°)		
O(5)-C(13)-C(12)	116.80(2)	117.19
C(4)-C(3)-C(2)	119.1(2)	119.56
N(1)-C(8)-C(9)	120.6(2)	120.25
C(8)-N(1)-C(7)	122.3(2)	123.02
N(1)-C(7)-C(2)	119.45(2)	119.05
N(1)-C(7)-C(6)	120.0(2)	120.20
C(2)-C(7)-C(6)	120.5(2)	120.74
C(3)-C(2)-C(1)	122.8(2)	123.62
C(3)-C(2)-C(7)	119.4(2)	118.88
C(1)-C(2)-C(7)	117.7(2)	117.48
O(1)-C(6)-C(5)	125.75(2)	125.78
O(1)-C(6)-C(7)	116.41(2)	115.43
C(5)-C(6)-C(7)	117.8(2)	118.78

C(6)-C(5)-C(4)	121.7(2)	120.71
C(13)-C(12)-C(11)	114.19(2)	112.82
O(2)-C(10)-O(3)	122.9(2)	111.50
O(2)-C(10)-C(11)	119.82(2)	123.05
O(3)-C(10)-C(11)	117.28(2)	125.43
C(9)-C(1)-C(2)	120.2(2)	120.98
C(1)-C(9)-C(8)	119.7(2)	119.19
O(4)-C(13)-O(5)	119.3(2)	119.54
O(4)-C(13)-C(12)	123.9(2)	123.24
C(12)-C(11)-C(10)	115.16(2)	113.12
C(3)-C(4)-C(5)	121.4(2)	121.30
Torsion angle values (°)		
C(8)-N(1)-C(7)-C(2)	0.8(3)	0.0
C(8)-N(1)-C(7)-C(6)	178.4(2)	-179.9
N(1)-C(7)-C(2)-C(3)	-179.3(2)	-179.9
C(6)-C(7)-C(2)-C(3)	-0.1(3)	0.0
N(1)-C(7)-C(2)-C(1)	-0.2(3)	0.0
C(6)-C(7)-C(2)-C(1)	179.0(2)	179.9
N(1)-C(7)-C(6)-O(1)	0.8(3)	0.0
C(2)-C(7)-C(6)-O(1)	-178.4(2)	-179.9
N(1)-C(7)-C(6)-C(5)	-179.7(2)	179.9
C(2)-C(7)-C(6)-C(5)	1.1(3)	0.0
O(1)-C(6)-C(5)-C(4)	178.3(2)	180.0
C(7)-C(6)-C(5)-C(4)	-1.2(4)	0.0
C(3)-C(2)-C(1)-C(9)	178.6(3)	179.9
C(11)-C(12)-C(13)-O(5)	178.9(2)	177.7
C(1)-C(2)-C(3)-C(4)	-179.9(2)	-179.9
C(7)-C(2)-C(3)-C(4)	-0.8(4)	**0.0**
C(13)-C(12)-C(11)-C(10)	-178.6(2)	-60.8
O(2)-C(10)-C(11)-C(12)	2.8(3)	19.9
O(3)-C(10)-C(11)-C(12)	-177.7(2)	-161.0
C(2)-C(3)-C(4)-C(5)	0.7(4)	-0.02
C(6)-C(5)-C(4)-C(3)	0.3(4)	0.02
C(7)-N(1)-C(8)-C(9)	-0.6(4)	-0.1
C(1)-C(9)-C(8)-N(1)	-0.1(4)	0.0
C(11)-C(12)-C(13)-O(5)	-0.9(4)	3.3
C(2)-C(1)-C(9)-C(8)	0.7(4)	0.0
C(7)-C(2)-C(1)-C(9)	-0.6(4)	**0.0**

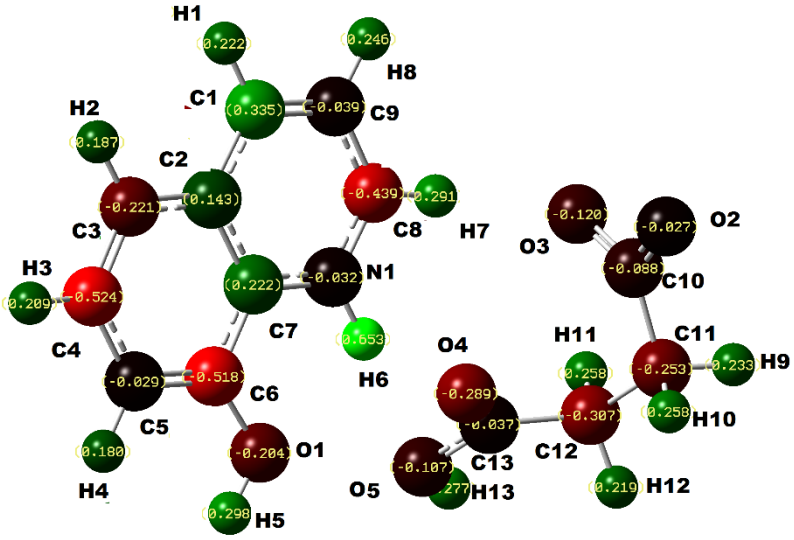

Figure 11. The Mulliken atomic charge distribution of OXSU.

Table 6. The calculated Mulliken atomic charge distribution of OXSU

Atoms	Charges	Atoms	Charges
C1	0.335	O4	-0.289
C2	0.143	O5	-0.107
C3	-0.221	N1	-0.032
C4	-0.524	H1	0.222
C5	-0.029	H2	0.187
C6	-0.518	H3	0.209
C7	0.222	H4	0.180
C8	-0.439	H5	0.298
C9	-0.039	H6	0.653
C10	-0.088	H7	0.291
C11	-0.253	H8	0.246
C12	-0.307	H9	0.233
C13	-0.037	H10	0.258
O1	-0.204	H11	0.258
O2	-0.027	H12	0.219
O3	-0.120	H13	0.277

The 3-carboxypropanoate anion moiety showed negative charges on all carbon (C10-C12) atoms. Similarly, all hydrogen (H1-H13) atoms of OXSU carried positive charges among them H5, H6 and H13 which displayed higher positive values. Remarkably the nitrogen (N1) and oxygen (O2) exhibited higher negative charges confirm their participation interactions such as N1—H8···O2 and O1—H7···O2 as evidenced by crystallographic data [25]. Consequently, these non-covalent interactions stabilize the supramolecular architecture, which ensures efficient charge transfer pathways between donor and acceptor orbitals. This ICT mechanism is a well-known technique to enhance second-order NLO responses [44].

4.8 Frontier molecular orbitals

The frontier molecular orbital (FMO) distribution of OXSU (Figure 12) provides an excellent indication of its electronic properties as well as its potential as NLO material. The HOMO is almost entirely localized over the quinolinium ring, and the LUMO is primarily located over the 3-carboxypropanoate group, indicating a clear D-A pair and a potential ICT pathway [45]. These important features increase the molecular hyperpolarizability (β) of OXSU thereby controlling the second order NLO efficiency [46]. The relatively low HOMO-LUMO energy gap of 3.87 eV suggests weak electronic excitation as polarization under the external field, which is a favorable requirement of a material to generate SHG [47]. The next orbitals to higher energy, HOMO–1 and LUMO+1, had a much lower delocalization gap of 6.39 eV which will also be contributing to the overall polarizability. The electron delocalization is facilitated by the hydrogen bonds with N1–H1···O2 and O1–H7···O2 interactions in the molecule. The results of Mulliken charge (Table 6) show that the electrostatic attraction between the N1 and the O1 of the (N1–H8 and O1–H7 respectively) hydrogen bonds effectively hold the charge together and facilitating the charge redistribution from HOMO to LUMO. In addition to all the structural convenience from the hydrogen bonds, they further establish elongated electronic pathways necessary to facilitate ICT and increase NLO response [48]. Finally, the directional hydrogen bonds will be useful to maintain the NCS in the molecular packing which are essential to the macroscopic observation of second order NLO response of OXSU [49].

4.9 Molecular electrostatic potential map analysis

In order to map reactive sites and polarity distribution, MEP surface of OXSU was computed according to B3LYP/6-311++G (d,p) basis set. MEP surface of OXSU quantifies regional polarity, identifies electrophilic/nucleophilic reactivity centers while simultaneously illustrates molecular geometry and dipole moment as shown in Figure 13. The regions of negative potential indicated by red shades correspond to the electron rich zones that are attributable to the electrophilic attack. While the positive potential indicated by blue shades corresponds to the electron deficient zones that are attributable to the nucleophilic attack.

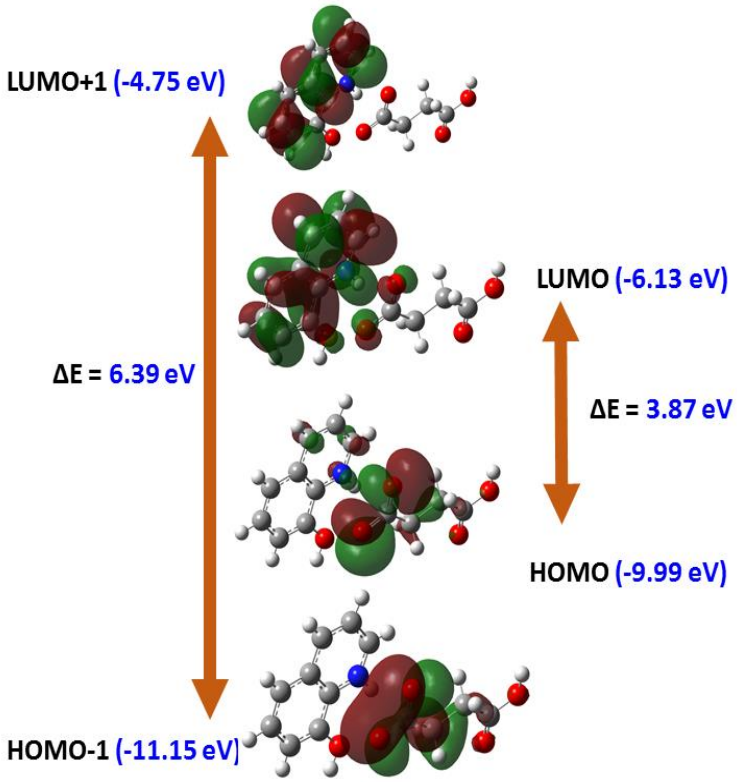

Figure 12. DFT calculated frontier molecular orbitals (HOMO and LUMO) for OXSU (iso-value = 0.02 a.u.)

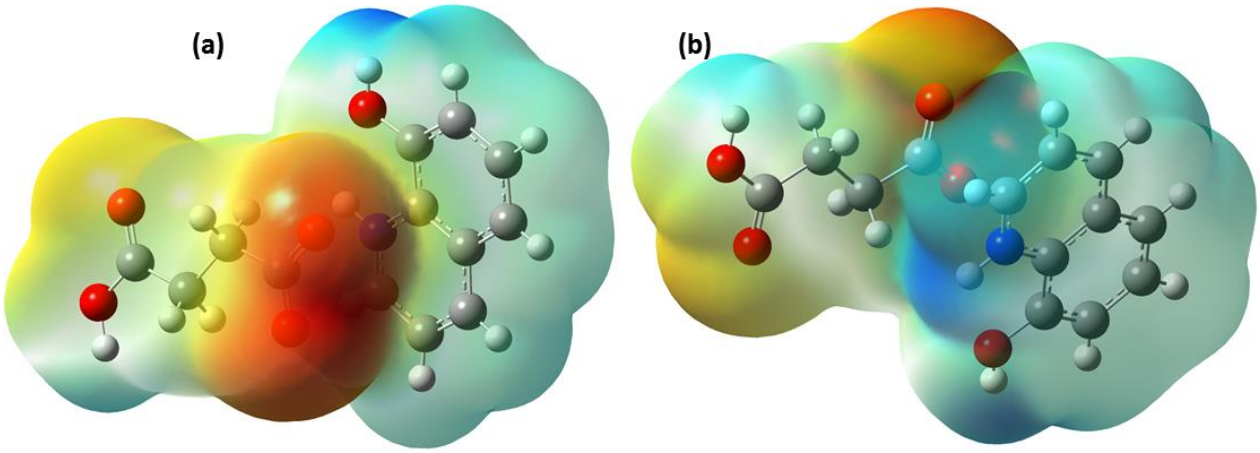

Figure 13. Orthogonal views of MEP surface of OXSU: **(a)** orientation A and **(b)** orientation B. Color gradient: red → orange → yellow → green → blue (increasing potential)

Intense negative MEP regions located at 3-carboxypropanoate carboxylate oxygen (O2 and O3) designating them as preferred nucleophilic centers for electrophile coordination. While hydrogen (H6 and H13) atoms of oxyquinolinium cation display solid positive potential, making them as key location for nucleophilic interactions. These observations consistent with the crystallographic investigations which confirm the participation of O2/O3 (carboxylate) and H6/H13 atoms in N–H···O, O–H···O and C–H···O interactions.

4.10 NBO Analysis

NBO study of OXSU highlights prominent electronic delocalization such as hyperconjugative effects, ICT phenomena, and strong hydrogen bonding, which synergistically contributes to its improved second order NLO response [50]. The evaluation of atomic charge distribution and orbital occupancies plays a pivotal role in characterizing the ICT mechanism in the system. Mulliken population analysis demonstrated that OXSU molecule exhibits well-defined charge localization characterized by the positively charged oxyquinolinium unit and negatively charged 3-carboxypropanoate unit. The quinolinium nitrogen (N19) atom, a formal N^+ species, exhibits large electron density. The large electron density on this atom represents a high degree of π-delocalization and polarization within the heteroaromatic system. This electron-rich character for a formally positive nitrogen confirms the strong

intramolecular charge transfer from the electron-donating oxy group and the anionic succinate moiety. It significantly reduces the positive charge on the quinolinium ring. This polarization highly influences the second-order NLO response of the material. In contrast, the oxygen atoms (O14) of the anion moiety exhibits high-occupancy lone pairs that can be involved in intermolecular interactions. The presence of low-occupancy core orbitals on certain carbon atoms (C4, C7, C8, C9) suggests minor electron delocalization effects, which may further influence the molecular polarizability. The NBO analysis identifies several bonding (σ) and antibonding (σ*) orbitals, with significant occupancies indicating strong hyperconjugative interactions. The C1–C2 bond (σ(1)) shows a 50% contribution from each carbon, with hybridizations of sp1.64 and sp1.98, respectively, suggesting strong σ-conjugation. The C1–N19 bond (σ(1)) exhibits a 36.83% contribution from C1 (sp^2.45 hybridized) and 63.17% from N19 (sp1.77 hybridized), indicating significant electron density delocalization from nitrogen to the carbon framework. This delocalization is further supported by the lone pair (LP) on nitrogen, which can conjugate with the π-system of the quinolinium ring, enhancing ICT. The second-order perturbation theory clearly reveals key D-A interactions, such as LP(N)→π*(C=C) or LP(O)→σ*(O-H), which significantly influence the enhancement of molecular hyperpolarizability (β). NBO study reveals the N–H···O and O–H···O intermolecular interaction between the cation and anion which are significantly sustaining the asymmetric crystal packing and enhancing the NLO behavior. The high lone pair occupancy of oxygen (O14 and O15) atoms serves as hydrogen bond acceptors. The linked hydrogen atoms (H25 and H32) display charges in the range of ~0.48–0.49 suggesting strong polarization featured by hydrogen bond formation. The O–H···O interaction is recognized by electron delocalization from the σ(O–H) orbital of the donor to the σ*(O–H) antibonding orbital of the acceptor leading the further stabilization. The NBO results correlate well with the observed NLO behavior of oxyquinolinium 3-carboxypropanoate. The significant charge separation and ICT between the quinolinium and 3-carboxypropanoate moieties lead to a large dipole moment, as reflected in the NBO-derived Mulliken charges [51]. This is essential for second-order NLO effects. One important factor influencing SHG efficiency is molecular hyperpolarizability (β), which is improved by the delocalization of lone pairs and π-electrons. Non-zero macroscopic susceptibility is ensured by the NCS alignment of the molecular dipoles caused by the N–H···O and O–H···O interactions ($\chi^{(2)}$) [52]. The significance of electronic delocalization, hyperconjugation, and hydrogen bonding in NLO activity of OXSU is highlighted by the NBO analysis. Accordingly, the combination of these factors leads to a significantly polarized and asymmetrical electronic structure of this material which could be utilized for applications such as frequency doubling, electro-optic modulation, and other NLO applications.

4.11 NLO calculations

The first-order hyperpolarizability (β) is a critical measure for second order NLO activity of a molecule. For OXSU, β_{total} = 16942.61 x 10^{-33} esu (Table 8) is greatly enhanced relative to benchmarks urea and p-nitroaniline, suggesting strong NLO activity. The improvement in β is due to a strong contribution of ICT between the oxyquinolinium donor and the 3-carboxypropanoate acceptor. Interestingly, the 3.87 eV energy for the HOMO-LUMO gap was calculated to result in low-energy excitation for this molecule. This supports the increased electronic polarizability of the modified OXSU system. The largest component of the hyperpolarizability tensor will often dominate the total hyperpolarizability value.

Table 7. Second-order perturbation theory analysis of Fock matrix in NBO basis including the stabilization energies using DFT at B3LYP/6-311++G (d,p) level.

Donor (i)	ED(i) (e)	Acceptor (j)	ED(j) (e)	E(2) (kJ/mol)	E(i)-E(j) (a.u.)	F(i, j) (a.u.)
π(05–N4)	1.9874	π*(05–N4)	0.6184	31.23	1.34	0.22
π(C6–C7)	1.6003	π*(C9–C8)	0.389	99.69	1.09	0.3
σ(C6–C7)	1.6003	π*(C10–C11)	0.2789	79.26	1.3	0.28
σ(C9–C10)	1.9761	σ*(C9–C8)	0.023	20.18	5.36	0.29
π(C9–C8)	1.6497	σ*(C9–C10)	0.0229	10.14	5.36	0.29
π(C9–C8)	1.6497	π*(05–N4)	0.6184	112.75	0.59	0.25
π(C9–C8)	1.6497	π*(C6–C7)	0.337	73.65	1.3	0.28
π(C10–C11)	1.6363	π*(C9–C8)	0.389	79.17	1.21	0.29

Table 8. The calculated electric dipole moment (μ_0), mean polarizability (α_0) and first order hyperpolarizability (β_{total}) components of the OXSU molecule

α components (x 10^{-24} esu)		β components (x 10^{-33} esu)	
α_{xx}	82.12	β_{xxx}	-465.03
α_{xy}	5.81	β_{xxy}	-11180.70
α_{yy}	30.19	β_{xyy}	2461.47
α_{xz}	4.57	β_{yyy}	-3779.21
α_{yz}	-0.69	β_{xxz}	-85.68
α_{zz}	19.75	β_{xyz}	1536.38
α_0	297.44	β_{yyz}	-1112.77
μ_x	-11.36	β_{xzz}	1548.09
μ_y	-8.07	β_{yzz}	-910.38
μ_z	-2.85	β_{zzz}	-1033.01
μ_0	14.22	β_{total}	16942.61

Whereas β_{xxy} component (−11180.70 x 10^{-33} esu) is the largest, along with its significant dipole moment oriented along the x-axis (μ_x = −11.36 D). Since mean polarizability is given as α_0 = 297.44x10^{-24} esu, suggest a strong response to an electric field. Hydrogen bonds N1−H1···O2 and O1−H7···O2 play an important role in inducing electron delocalization. Hydrogen bonds also facilitate NCS packing of neighboring molecules, both of which may play a role in enabling SHG [53]. NCS packing permits directional charge flow and alignment of dipoles between cation and anion. The high β_{total} values, while supporting the desired orientation of the OXSU orbitals, predictable charge transfers, and with assistance from hydrogen bonds. It implies that OXSU is a promising second-order NLO material for photonic and optoelectronic uses. Urea is commonly used as a standard reference for assessing NLO characteristics of organic materials. The first hyperpolarizability (β_0) of urea was computed as 0.51 x10^{-30} esu. The first hyperpolarizability (β) of OXSU is 16.94 x 10^{-30} esu, which is 33-fold enhancement relative urea. This highlights the candidature of OXSU as a promising second-order NLO material.

5. Conclusion

In summary, this work presents a comprehensive investigation of NLO properties of OXSU by using both experimental and computational methods. SCXRD unequivocally establishes that OXSU crystallizes NCS, $P2_1$, space group, an essential criterion for second-order NLO activity. According to the HS analysis, the acentric crystal architecture of OXSU, which is stabilised by a synergistic cooperation of strong N1—H8···O2 and O1—H7···O2 hydrogen bonds, weaker C–H···O contacts, and dominant van der Waals (H···H) interactions. Spectroscopic (FTIR and Raman) analysis confirms the nature of charge transfer interaction and hydrogen bonding which also confirms the structural stability of the crystal. ICT between the electron-rich oxyquinolinium cation and the 3-carboxypropanoate anion in a way of π-conjugation leads to extremely small HOMO-LUMO energy gap (3.82 eV) which is responsible for significant increase in electronic polarizability and NLO response. The strong dipole moment and charge transfer properties of the material suggest significant electronic asymmetry. This is further evidenced by Mulliken charge distribution and NBO analysis. MEP analysis also reveals strong charge asymmetry in OXSU, with electron-rich carboxylate oxygens and electron-deficient hydrogens driving its NLO activity. The first-order hyperpolarizability (β_{total} = 16.94 x 10^{-30} esu) of OXSU is 33 times greater than that of urea. The SHG efficiency of OXSU is 1.3 times higher than KDP, demonstrating the excellent phase matching NLO performance. This work significantly advances the understanding of the SP relationship of OXSU and establishes the foundation for the design of novel organic NLO materials towards future-generation optoelectronic device application.

References

[1] J.K. Zaręba, M. Nyk, M. Samoć, Nonlinear optical properties of emerging nano-and microcrystalline materials. Advanced Optical Materials, 9(23), (2021) 2100216. https://doi.org/10.1002/adom.202100216

[2] O. Dogadov, C. Trovatello, B. Yao, G. Soavi, G. Cerullo, Parametric nonlinear optics with layered materials and related heterostructures. Laser & Photonics Reviews, 16(9) (2022) 2100726. https://doi.org/10.1002/lpor.202100726

[3] W. Huang, Y. Xiao, F. Xia, X. Chen, T. Zhai, Second harmonic generation control in 2D layered materials: status and outlook. Advanced

Functional Materials, 34(16), (2024) 2310726. https://doi.org/10.1002/adfm.202310726

[4] F. Castet, C. Tonnelé, L. Muccioli, B. Champagne, Predicting the second-order nonlinear optical responses of organic materials: the role of dynamics. Accounts of chemical research, 55(24), (2022) 3716-3726. https://doi.org/10.1021/acs.accounts.2c00616

[5] T. Radhakrishnan, Molecular structure, symmetry, and shape as design elements in the fabrication of molecular crystals for second harmonic generation and the role of molecules in-materials. Accounts of chemical research, 41(3), (2008) 367-376. https://doi.org/10.1021/ar7002072

[6] R. Medishetty, J.K. Zaręba, D. Mayer, M. Samoć, R.A. Fischer, Nonlinear optical properties, upconversion and lasing in metal–organic frameworks. Chemical Society Reviews, 46(16), (2017) 4976-5004. https://doi.org/10.1039/C7CS00162B

[7] M. Khalid, M.U. Khan, I. Shafiq, R. Hussain, K. Mahmood, A. Hussain, R. Jawaria, A. Hussain, M. Imran, M.A. Assiri, NLO potential exploration for D–π–A heterocyclic organic compounds by incorporation of various π-linkers and acceptor units. Arabian Journal of Chemistry, 14(8), (2021) 103295.

[8] J. Wu, Z.a. Li, J. Luo, A.K.Y. Jen, High-performance organic second-and third-order nonlinear optical materials for ultrafast information processing. Journal of Materials Chemistry C, 8(43), (2020) 15009-15026. https://doi.org/10.1039/D0TC03224G

[9] A.U. Hassan, S.H. Sumrra, M. Zubair, G. Mustafa, M.F. Nazar, M.N. Zafar, Structurally modulated D-π-DA (Semiconductor) anchoring dyes to enhance the tunable NLO response: a DFT/TDDFT quest for new photovoltaic materials. Structural Chemistry. 34(3), (2023) 1043-1060. https://doi.org/10.1007/s11224-022-02070-3

[10] I.V. Fedyanin, Control of supramolecular chirality in co-crystals of achiral molecules via stacking interactions and hydrogen bonding. CrystEngComm, 24(14), (2022) 2591-2601. https://doi.org/10.1039/D2CE00081D

[11] P. Alivisatos, P.F. Barbara, A.W. Castleman, J. Chang, D.A. Dixon, M.L. Klein, G.L. McLendon, J.S. Miller, M.A. Ratner, P.J. Rossky, from molecules to materials: Current trends and future directions. Advanced Materials, 10(16), (1998) 1297-1336. https://doi.org/10.1002/(SICI)1521-4095(199811)10:16%3C1297::AID-ADMA1297%3E3.0.CO;2-7

[12] E. Shobhana, B. Balraj, R. Kannan, R. Thirumurugan, Synthesis and physiochemical investigations of imidazolium 4-hydroxybenzoate (I4HB) for nonlinear optical applications. Indian Journal of Chemistry (IJC), 63(6), (2024) 572-578. https://doi.org/10.56042/ijc.v63i6.8855

[13] C. Wang, T. Zhang, W. Lin, Rational synthesis of noncentrosymmetric metal–organic frameworks for second-order nonlinear optics. Chemical Reviews, 112(2), (2012) 1084-1104. https://doi.org/10.1021/cr200252n

[14] J. Zhang, X. Li, Intramolecular hydrogen bonding, π-π stacking interactions, and substituent effects of 8-hydroxyquinoline derivative super molecular structures: A theoretical study. Journal of molecular modeling, 25(8), (2019) 241. https://doi.org/10.1007/s00894-019-4140-2

[15] M. Balón, P. Guardado, M.A. Muñoz, C. Carmona, A spectroscopic study of the hydrogen bonding and π–π stacking interactions of harmane with quinolone. Bio spectroscopy, 4(3), (1998) 185-195. https://doi.org/10.1002/(SICI)1520-6343(1998)4:3%3C185::AID-BSPY4%3E3.0.CO;2-3

[16] A. Franklin Ebenazer, M. Saravanabhanvan, N. Sampathkumar, S. Ramesh, M. Shabbir, A.R. Chaudhry, S.K. Lakkaboyana, H. Trilaksana, R.M.N. Kalla, J. Lee, P. Seepana, Synthesis, spectral, crystal structure, linear and NLO properties of quinoline Schiff base: Combined experimental and DFT calculations. Journal of Molecular Structure, 1324, (2025) 140781. https://doi.org/10.1016/j.molstruc.2024.140781

[17] R. Thirumurugan, B. Babu, K. Anitha, Exploring second-order NLO activity in imidazolium quinoline-2-carboxylate dihydrate (IQD): Synthesis, crystal engineering, spectral and DFT insights. Journal of Molecular Structure, 1351, (2026) 144130. https://doi.org/10.1016/j.molstruc.2025.144130

[18] H. Bouabbaci, A.K. Nacereddine, Effect of electronic nature of substituent position on the linear and nonlinear optical and physical properties of some quinoline derivatives: A computational study. Molecular Physics, 123(17), (2025). https://doi.org/10.1080/00268976.2025.2456112

[19] A. Jamal, M.S.H. Faizi, A.K. Roy, Synthesis, crystal structure, and spectroscopic study of a novel quinoline derivative with nonlinear optical activity and esterase inhibition potential. Journal of Molecular Structure, 1352, (2026) 144407. https://doi.org/10.1016/j.molstruc.2025.144407

[20] S.A. Aloudah, A.A. Fadda, E. Abdel-Latif, E. Nabil, M. Zakaria, Multifunctional D-π-A dyes featuring triphenylamine–quinoline architecture: Rational design for prospective photovoltaic and nonlinear optical performance. Journal of Molecular Structure, 1350, (2026) 144024. https://doi.org/10.1016/j.molstruc.2025.144024

[21] R. Wang, Y. Cao, D. Jia, L. Liu, F. Li, New approach to synthesize 8-hydroxyquinoline-

based complexes with Zn2+ and their luminescent properties. Optical Materials, 36(2), (2013) 232-237. https://doi.org/10.1016/j.optmat.2013.08.032

[22] G. Parvathy, R. Kaliammal, K. Velsankar, V. Mohankumar, K. Sankaranarayanan, S. Sudhahar, Physicochemical and computational perspectives of 8-hydroxyquinoline 5-chloro-2-hydroxybenzoic acid: a novel second-order nonlinear optical crystal. Applied Physics A, 127(12), (2021) 957. https://doi.org/10.1007/s00339-021-05115-2

[23] G. Peramaiyan, P. Pandi, N. Vijayan, G. Bhagavannarayana, R.M. Kumar, Crystal growth, structural, thermal, optical and laser damage threshold studies of 8-hydroxyquinolinium hydrogen maleate single crystals. Journal of crystal growth, 375, (2013) 6-9. https://doi.org/10.1016/j.jcrysgro.2013.04.011

[24] M.D. Halls, H.B. Schlegel, Molecular orbital study of the first excited state of the OLED material tris (8-hydroxyquinoline) aluminum (III). Chemistry of materials, 13(8), (2001) 2632-2640. https://doi.org/10.1021/cm010121d

[25] R. Thirumurugan, B. Babu, K. Anitha, J. Chandrasekaran, Investigation on growth, structure and characterization of succinate salt of 8-hydroxyquinoline: an organic NLO crystal. Spectrochimica Acta Part A: Molecular and Biomolecular Spectroscopy, 140 (2015) 44-53. https://doi.org/10.1016/j.saa.2014.12.093

[26] M. Khalid, M. Khan, K. Mahmood, M. Arshad, M. Imran, A.A.C. Braga, R. Hussain, Theoretical designing of non-fullerene derived organic heterocyclic compounds with enhanced nonlinear optical amplitude: a DFT based prediction. Scientific Reports, 12(1), (2022) 20220. https://doi.org/10.1038/s41598-02221894-x

[27] S. Chatterjee, M. Afzal, P.C. Mandal, R. Modak, M. Guin, S. Konar, Exploration of supramolecular interactions, Hirshfeld surface, FMO, molecular electrostatic potential (MEP) analyses of pyrazole based Zn (II) complex. Journal of the Indian Chemical Society, 101(10), (2024) 101275. https://doi.org/10.1016/j.jics.2024.101275

[28] M. Guin, S. Halder, S. Chatterjee, S. Konar, Synthesis, X-ray crystal structure of Cu (II) 1D coordination Polymer: In View of Hirshfeld surface, FMO, Molecular electrostatic potential (MEP) and Natural Bond orbital (NBO) analyses. Journal of Molecular Structure, 1270, (2022) 133949. https://doi.org/10.1016/j.molstruc.2022.133949

[29] Enraf-Nonius, CAD-4 EXPRESS Version 5.1/1.2, Enraf-Nonius, Delft, 1994.

[30] M.J.E.A. Frisch, (2009). gaussian 09, Revision d. 01, Gaussian. *Inc, Wallingford CT*, *201*.

[31] R. Dennington, T.A. Keith, J.M. Millam, (2016). GaussView 6.0. 16. *Semichem Inc.: Shawnee Mission, KS,* USA.

[32] J.J. McKinnon, F.P.A. Fabbiani, M.A. Spackman, Comparison of Polymorphic Molecular Crystal Structures through Hirshfeld Surface Analysis. Crystal Growth & Design, 7(4), (2007) 755-769. https://doi.org/10.1021/cg060773k

[33] X. Liu, Y.C. Yang, M.Y. Li, L. Chen, L.M. Wu, Anisotropic structure building unit involving diverse chemical bonds: a new opportunity for high-performance second-order NLO materials. Chemical Society Reviews, 52(24), (2023) 8699-8720. https://doi.org/10.1039/D3CS00691C

[34] L. Jensen, L. Zhao, J. Autschbach, G. Schatz, Theory and method for calculating resonance Raman scattering from resonance polarizability derivatives. The Journal of chemical physics, 123(17), (2005). https://doi.org/10.1063/1.2046670

[35] V. Krishnakumar, R. Ramasamy, DFT studies and vibrational spectra of isoquinoline and 8 hydroxyquinoline. Spectrochimica Acta Part A: Molecular and Biomolecular Spectroscopy, 61(4), (2005) 673-683. https://doi.org/10.1016/j.saa.2004.05.030

[36] E. Shobhana, R. Kesavasamy, H. Arul, R. Thirumurugan, B. Babu, Synthesis, structural, hirshfeld, spectral, thermal, Z-scan analysis and computational studies of 4-chloroanilinium quinoline-2-carboxylate (4CQ). Journal of molecular structure, 1204, (2020)127516. https://doi.org/10.1016/j.molstruc.2019.127516

[37] R. Thirumurugan, S. Priyadharshini, B. Babu, B.M. Babu, K. Anitha, An efficient phase matching second harmonic generation of 2-amino-4-methylpyridinium quinoline-2-carboxylate (C16H15N3O2) organic single crystal: Structural, optical, thermal, and computational investigations. Journal of Molecular Structure, 1332, (2025) 141453. https://doi.org/10.1016/j.molstruc.2025.141453

[38] A. Shafiq, M. Adnan, R. Hussain, Z. Irshad, U. Farooq, S. Muhammad, Molecular engineering of anthracene core-based hole-transporting materials for organic and perovskite photovoltaics. ACS omega, 8(39), (2023) 35937-35955. https://doi.org/10.1021/acsomega.3c03790

[39] H. Cheng, W. Jin, Z. Yang, S. Pan, Performance of optical materials with the derivative of planar π-conjugated groups: Recent advances and future prospects. Inorganic Chemistry Frontiers, 9(17), (2022) 4554-4568. https://doi.org/10.1039/D2QI00990K

[40] T.C. Lin, J.M. Cole, A.P. Higginbotham, A.J. Edwards, R.O. Piltz, J. Perez-Moreno, J.Y. Seo, S.C. Lee, K. Clays, O.P. Kwon, Molecular origins of the high-performance nonlinear optical

susceptibility in a phenolic polyene chromophore: electron density distributions, hydrogen bonding, and ab initio calculations. The Journal of Physical Chemistry C, 117(18), (2013) 9416-9430. https://doi.org/10.1021/jp400648q

[41] A. Haque, K.M. Alenezi, M.S. Khan, W.-Y. Wong, P.R. Raithby, Non-covalent interactions (NCIs) in π-conjugated functional materials: advances and perspectives.Chemical Society Reviews, 52(2), (2023) 454-472. https://doi.org/10.1039/D2CS00262K

[42] T. Lerdwiriyanupap, R. Cedeno, P. Nalaoh, S. Bureekaew, V. Promarak, A.E. Flood, Enantiopurification of Mandelic Acid by Crystallization-Induced Diastereomer Transformation: An Experimental and Computational Study, Crystal Growth & Design, 23(3), (2023) 2001-2010. https://doi.org/10.1021/acs.cgd.2c01551

[43] E.U. Mughal, S.F. Kainat, A.M. Almohyawi, N. Naeem, E.M. Hussein, A. Sadiq, A. Abd-El-Aziz, N. Ma, A.S. Abd-El-Aziz, A. Timoumi, Thermally activated delayed fluorescence materials: innovative design and advanced application in biomedicine, catalysis and electronics. RSC advances, 15(10), (2025) 7383-7471. https://doi.org/10.1039/D5RA00157A

[44] S.W. Yang, A. Elangovan, K.C. Hwang, T.I. Ho, Electronic polarization reversal and excited state intramolecular charge transfer in donor/acceptor ethynylpyrenes. The Journal of Physical Chemistry B, 109(35), (2005) 16628-16635. https://doi.org/10.1021/jp052086u

[45] M.U. Khan, M. Ibrahim, M. Khalid, A.A.C. Braga, S. Ahmed, A. Sultan, Prediction of second-order nonlinear optical properties of D–π–A compounds containing novel fluorene derivatives: A promising route to giant hyperpolarizabilities. Journal of Cluster Science, 30(2), (2019) 415-430. https://doi.org/10.1007/s10876-018-01489-1

[46] S. Nadeem, A. Anwar, M.U. Khan, M. Idrees, M.A. El-Tayeb, M.A. Ibrahim, Unveiling charge transfer kinetics and static-dynamic nonlinear optical switching in 2-phenylthiophene push-pull chromophores: DFT-based theoretical modelling for enhanced harmonic generation and electro-optic applications, Journal of Molecular Graphics and Modelling,(2025)109061. https://doi.org/10.1016/j.jmgm.2025.109061

[47] S. Semin, X. Li, Y. Duan, T. Rasing, Nonlinear optical properties and applications of fluorenone molecular materials. Advanced Optical Materials, 9(23), (2021) 2100327. https://doi.org/10.1002/adom.202100327

[48] Q. Li, Z. Li, Molecular packing another key point for the performance of organic and polymeric optoelectronic materials. Accounts of Chemical Research, 53(4), (2020) 962-973. https://doi.org/10.1021/acs.accounts.0c00060

[49] I. Kaifi, S. Muhammad, S. Bibi, S. Urrehman, A. Kalam, A.R. Chaudhry, S.S. Alarfaji, A.G. Al-Sehemi, Optimizing Core Modifications for High-Performance D-A-D Molecular Systems: a Multi-Faceted Study on NLO Properties, Solvent Effects, Charge Transfer, and Photovoltaic Efficiency. Advanced Theory and Simulations, (2025) 2500169. https://doi.org/10.1002/adts.202500169

[50] J.H. Jeong, J.S. Kim, J. Campo, S.H. Lee, W.Y. Jeon, W. Wenseleers, M. Jazbinsek, H. Yun, O.P. Kwon, N-Methylquinolinium derivatives for photonic applications: Enhancement of electron-withdrawing character beyond that of the widely used N-methylpyridinium. Dyes and Pigments, 113, (2015) 8-17. https://doi.org/10.1016/j.dyepig.2014.07.016

[51] A. Datta, S.K. Pati, Dipolar interactions and hydrogen bonding in supramolecular aggregates: understanding cooperative phenomena for 1st hyperpolarizability. Chemical Society Reviews, 35(12), (2006) 1305-1323. https://doi.org/10.1039/B605478A

[52] X. Shi, W. Bao, Hydrogen-bonded conjugated materials and their application in organic field-effect transistors. Frontiers in Chemistry, 9, (2021) 723718. https://doi.org/10.3389/fchem.2021.723718

[53] D. Pant, S. Sitha, Roles of bridges on electronic, linear and nonlinear optical properties: a computational study on zwitterions with N-methyl pyridinium and p-dicyanomethanide phenylene. Computational and Theoretical Chemistry, 1229, (2023) 114308. https://doi.org/10.1016/j.comptc.2023.114308

Authors Contribution Statement

R. Thirumurugan: Conceptualization, Methodology, Data curation, Formal analysis, Validation, Writing – Original Draft, Writing – Review and Editing. K. Raju: Software validation, Writing – Review and Editing. K. Moovendaran: Writing – Original Draft, Writing – Review and Editing. E. Shobhana: Writing – Original Draft, Writing review and editing. All the authors read and approved the final version of the manuscript.

Funding

The authors declare that no funds, grants or any other support were received during the preparation of this manuscript.

Competing Interests

The authors declare that there are no conflicts of interest regarding the publication of this manuscript.

Has this article screened for similarity?

Yes

Data Availability

The data supporting the findings of this study can be obtained from the corresponding author upon reasonable request.

About the License